Memoirs of the Faculty of Science, Kyoto University, Series of Physics, Astrophysics, Geophysics and Chemistry, Vol. XXXVI, No. 1, Article 5, 1981

MEASUREMENT OF THE POLARIZATION PARAMETERS FOR THE $\pi^-p\to\pi^0n$ CHARGE EXCHANGE SCATTERING IN THE MOMENTUM REGION BETWEEN 1.965 AND 2.960 GeV/c

By

Makoto MINOWA

(*Received March 17, 1979*)

ABSTRACT

Polarization parameters for the $\pi^-p\to\pi^0n$ scattering were measured at five momenta of 1.965, 2.168, 2.360, 2.566 and 2.690 GeV/c in the angular range between $\cos\theta^*=-0.90$ and 0.95. Characteristics of this experiment were the use of 174 lead glass counters for the measurement of both directions and energies of the γ-rays from the decay of the π^0 meson, and the use of 118 plastic scintillation counters for the detection of the recoil neutron. A polarized proton target was used with polarizations achieved ranging from 60% to 70%. The results were compared with the predictions by the Regge pole model and the recent π-N phase shift solutions. The prediction by the Regge pole model does not reproduce the present results. The discrepancies with the Karlsruhe-Helsinki phase shift analysis are discussed in detail.

I. Introduction

Pion-nucleon scattering have been studied experimentally and theoretically for many years, and plenty of data have been accumulated for three kinds of pion-nucleon scatterings:

$$\pi^+p \longrightarrow \pi^+p, \tag{1}$$

$$\pi^-p \longrightarrow \pi^-p, \tag{2}$$

$$\pi^-p \longrightarrow \pi^0n. \tag{3}$$

The scattering amplitudes for these scatterings can be written in the form:

$$A_q=f_q+ig_q\sigma\cdot\boldsymbol{n}, \text{ (for } q=+,\ -\text{ and } 0), \tag{4}$$

where σ is the Pauli's spin matrix vector and $\boldsymbol{n}$ is the normal to the scattering plane. f and g are the spin-nonflip and spin-flip amplitudes, respectively. The lower indices $+$, $-$ and 0 correspond to the scattering (1), (2) and (3), respectively. A differential cross section $d\sigma/d\Omega$ and a polarization parameter P are expressed with f and g as follows;

$$d\sigma/d\Omega=|f|^2+|g|^2, \tag{5}$$

$$P=-2\,\mathrm{Im}\,(f^*\cdot g)/(|f|^2+|g|^2). \tag{6}$$

As is seen in these equations, the polarization parameter is correlated to the relative phase difference between the amplitudes f and g, while the differential cross section

does not depend on it. Therefore, measurements of the polarization parameters offer useful informations independent of those obtained from measurements of the differential cross sections.

The amplitudes f and g for each kind of scattering can be decomposed into s-channel isospin 1/2 and 3/2 amplitudes as follows;

$$T_+ = T(3/2), \tag{7}$$

$$T_- = 1/3 \cdot [T(3/2) + 2T(1/2)], \tag{8}$$

$$T_0 = \sqrt{2}/3 \cdot [T(3/2) - T(1/2)], \tag{9}$$

where T stands for either f or g. Therefore, one has to determine four complex amplitudes of $f(1/2)$, $g(1/2)$, $f(3/2)$ and $g(3/2)$ at each energy and angle in order to describe the pion-nucleon scattering completely. Since a common phase among these complex amplitudes is meaningless, seven independent quantities have to be determined experimentally. However, at most six observables, differential cross sections and polarization parameters for the scattering (1), (2) and (3), can be available in the resonance region, because spin-rotation data have not been measured systematically. Therefore, the scattering amplitudes cannot be determined directly without some theoretical constraints.

The phase shift analysis has been performed extensively for pion-proton scattering to clarify the behaviors of the partial waves, and has led to the investigation of many non-strange baryon resonances. The existence of these many resonances became the strong support of the quark models of hardrons, and these baryon resonances are successfully classified into the $SU(6) \times O(3)$ multiplets[1]. However, there still remain some ambiguities even in the recent phase shift analyses[2)3)4)]. These ambiguities mainly come from imprecise or inconsistent data and also from rather poor accummulation of data for the scattering (3), which we call the charge exchange scattering.

Moreover, the charge exchange scattering is particularly important, since its amplitudes can be written as the difference between isospin 3/2 and 1/2 amplitudes, as is seen in Equation (9). Therefore, it is expected to be sensitive to the resonances in either isospin states.

Fig. 1 shows the present status of the data accumulation in the world between 1.5 and 3.5 GeV/c for the polarization parameters of the charge exchange scattering. In this energy region, measurements of the polarization parameters are very scarce, especially above 2 GeV/c, while those of the differential cross sections are fairly abundant. In the high momentum region above 2.3 GeV/c, existing data of the polarization parameters are limited only at the forward angular regions. It is considered that Regge pole models can explain high energy scatterings at the forward and the backward angular region. At ANL[5),6)] and CERN[7),8)], the forward polarization parameters were measured at 2.07, 2.50, 2.72, 3.20, 3.47, 3.50, 4.90, 5.00, 5.90, 7.85 and 11.20 GeV/c in order to test the Regge pole models.

On the other hand, measurements at all angular region are necessary in order to perform the phase shift analyses. Since there are still many resonances and candidates in this energy region, as are also shown in Fig. 1, the precise phase shift analyses are still important to establish s-channel resonances above 2 GeV/c. Recently, at LBL[9),10)] and the Rutherford Laboratory[11),12)], both of the differential cross sections and the polarization parameters for the charge exchange scattering at almost all angles were measured up to 1.790 GeV/c and 2.267 GeV/c, respectively.

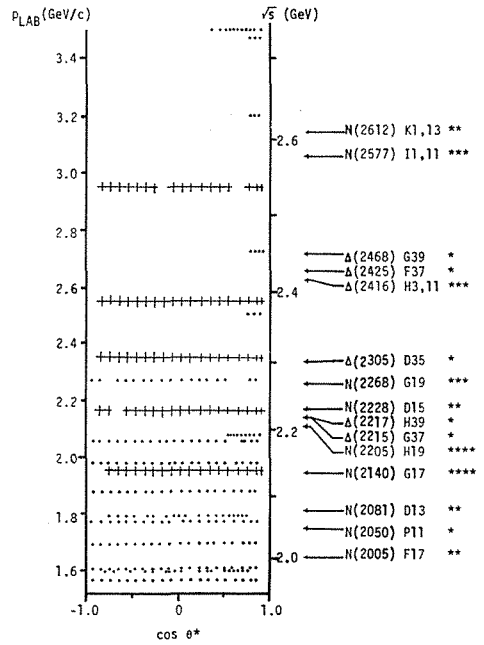

Fig. 1. The present status of experimental measurements of the polarization parameters for the π-N charge exchange scattering. Measured points of data accumulated up to now are indicated by dots together with those of the present measurement by crosses. Candidates for the π-N resonances are also indicated in the notation of the Particle Data Group on the right according to the Karlsruhe-Helsinki 78 solution.

In the present experiment, which was performed as the first counter experiment at KEK†, precise and systematic measurements of both of the differential cross sections and the polarization parameters have been done at the new momentum region between 1.965 and 2.960 GeV/c at almost all angles. One of the purposes of this experiment is to extend the systematic measurements of the differential cross sections and the polarization parameters up to high momentum region in order to remove the ambiguities from the phase shift analyses in this energy region.

The results on the polarization parameters are given in this paper. The results on the differential cross sections are presented elsewhere[13].

II. Experiment

A. General

The experimental set up is shown in Fig. 2. The negative pion beam was focused on a polarized proton target constructed by the Polarized Target Group of KEK. Because ethylene glycol was used as a target material, there were heavy nuclei in the target and the surrounding cavity wall and cylinders of a cryostat besides the free protons in ethylene glycol. The quasi-elastic charge exchange scattering from the

† National Laboratory for High Energy Physics.

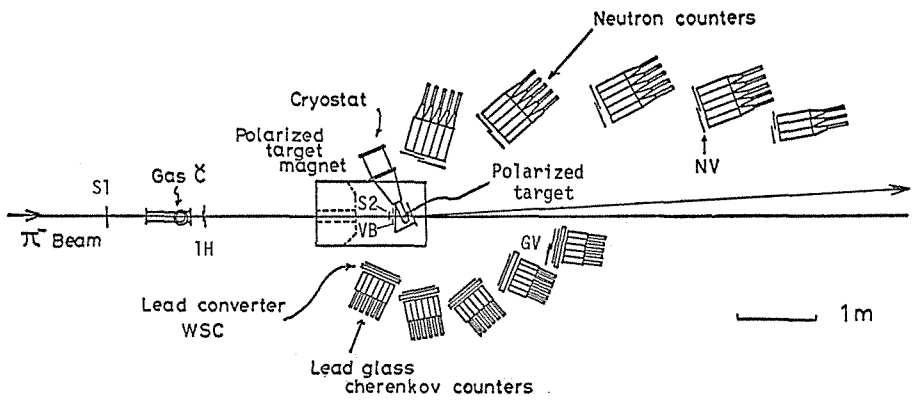

Fig. 2. A plan view of the experimental apparatus.

bound protons in these heavy nuclei were the serious background source. In order to reduce this background, both energies and directions of two γ-rays from the π° mesons were measured to evaluate the momentum and the scattering angle of the π° mesons with good precision. At the same time, the direction of recoil neutron was detected. Hence, the identification of the charge exchange scattering has been performed in a rather clear way than the measurements performed at other laboratories[9),10),11),12)].

The target was surrounded by an assembly of scintillation counters in order to assure that the reaction produced no charged particles in the final state. Tungsten sheets were inserted between these veto counters to veto such events that emitted γ-rays in directions other than towards the π°-detection system.

The energies and the scattering angles of the γ-rays from the π° mesons were measured with the π°-detection system consisting of five boxes. Each box had a matrix array construction of lead glass Cherenkov counters of total absorption type. In front of each box, there was an assembly of a lead sheet and a wire spark chamber stack, whose informations were partially used to test the performances of the system.

The gains and engergy resolutions of each lead glass counter were measured previous to the experiment by using monochromatic electrons contained in the pion beam, and re-calibrated after some long shut downs of the experiment. For these measurements, and internal target of tungsten was used instead of beryllium to increase the number of electrons in the pion beam. A drift of gains was monitored by means of light pulsers of light emission diodes which were attached to all counters.

Recoil neutrons were detected by 118 plastic scintillation counters. These counters were also mounted in five boxes having matrix array constructions. A veto counter was placed in front of each box to protect the neutron counters against to charged particles. Light emission diodes were also attached to all the neutron counters to monitor the drift of counter gains.

The electronic circuit system generated the trigger pulse whenever the following requirements were satisfied: 1) a negative charged pion hit the target; 2) no signals from the veto counters surrounding the target; 3) at least two lead glass counters had pulses above threshold level; 4) one or more neutron counters were fired without firing the veto counters in front of them. For each event, informations from these counters were stored into a PDP 11/45 computer via CAMAC system with A–D converters, parallel coincidence registers and scalers. These informations were then

recorded on magnetic tapes, and also partially analysed to monitor the performance of the apparatus. The informations were also sent to the KEK central computer system HITAC 8800 via KEK NET on-line network for further analyses of events. Target polarizations were measured automatically for every 17.5 seconds using a small computer OKITAC 4300b, and were transferred to the PDP 11/45 computer via CAMAC transmitter/receiver modules.

The events were collected for the polarized target with spins up/down and for the carbon target. "Carbon target runs" were performed at each momentum to measure the background events from the bound protons. The polarization parameter was calculated from the formula:

$$P(\theta)=\frac{U(\theta)-D(\theta)}{P\uparrow\cdot D(\theta)-P\downarrow\cdot U(\theta)-(P\uparrow-P\downarrow)\cdot C(\theta)}\cdot\frac{1}{\langle\cos\phi\rangle}, \quad (10)$$

with $U(\theta)$, $D(\theta)$, $C(\theta)$ = the normalized numbers of events for the target spins up/down and for the carbon target, respectively.

$P\uparrow$, $P\downarrow$ = target polarizations for up and down; $P\uparrow$ is positive and $P\downarrow$ is negative in sign.

$\langle\cos\phi\rangle$ = cosine of azimuthal angle of the scattered π° meson averaged with the events.

In the case of $|P\uparrow|=|P\downarrow|=P_t$, it becomes well-known formula:

$$P(\theta)=\frac{1}{P_t\langle\cos\phi\rangle}\cdot\frac{U(\theta)-D(\theta)}{U(\theta)+D(\theta)-2\cdot C(\theta)}. \quad (11)$$

B. Beam

The negative pion beam produced at 10° from an internal beryllium target (1.0 mm in diameter and 15.0 mm long) of KEK–PS was transported to the experimental focal point called F1 as is shown in Fig. 3. The beam transporting system consisted of two stages, each stage having two bending magnets and two quadrupole magnets. At an intermediate focal point between the two stages, the momentum of the pion was selected by a horizontal lead collimator with an adjustable slit. There was also an adjustable vertical lead collimator which was used to limit the beam size. The momentum spread of the beam was adjusted to be 1% (FWHM) in the present experiment. The absolute beam momentum was calibrated by a time of flight measurement at 2.0 GeV/c with an accuracy of 0.2%. The focal point F1 was not designed to be dispersion free, therefore, the mementum dispersion at that point was $\frac{\Delta p}{p}/\Delta x=$ 5%/cm.The last bending magnet of the second stage, which was named D4, was followed by a polarizing magnet with wide aperture. Because the polarizing magnet deflects the beam, the magnetic field of D4 was slightly adjusted to center the beam on the polarized target. To do this, a small movable finger scintillation counter was inserted on the target position to confirm that the beam went through the center of the target.

The direction in which the beam travelled as it passed through the center of the target, which defined the "0° line" of a scattering, was measured by using another movable scintillation counter placed approximately 3.5 meters downstream the target. The beam center at that point was measured by sliding the movable counter, and joining this point with the center of the target, an "outgoing line" was defined. Then, an estimated "0° line" was defined as a bisector of this "outgoing line" and the

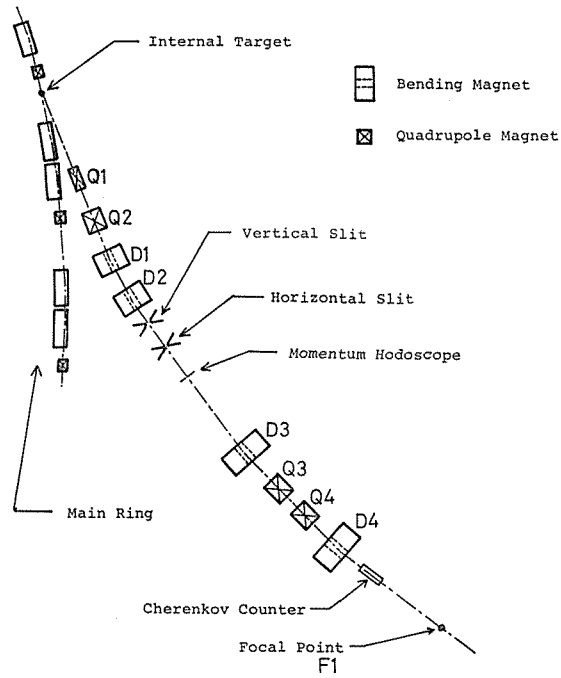

Fig. 3. The layout of the beam transport system.

incoming beam line. Although this estimate included some approximations, the measured deflection angle agreed with the value calculated from a magnetic field map of the polarizing magnet within an accuracy of 3%.

The beam profile was measured by using the finger counter mentioned above and by a film exposure. The beam size at the target was found to be typically 15 mm (FWHM) in vertical and horizontal directions. The beam intensity was ranging from 2 to $5\times10^5\pi^-$ per 10^{12} circulating protons of 8 GeV with the spill length of approximately 350 msec.

The contamination of the beam by muons and electrons will be described in the Section **II–D**.

C. Polarized Target

The polarized proton target used in this experiment was cooled with a ^{3}He refrigerator down to a temperature less than 0.5°K. The polarizing magnet provided a uniform field of 2.5 T over the target volume. Microwave pumping at a frequency of around 70 GHz induced dynamic polarization. A detailed description of this polarized target is given elsewhere[14], therefore, only the description specific in the present experiment follows.

The target material primarily consisted of ethylene glycol doped with chromium V complexes ($K_2Cr_2O_7$) frozen into small beads with a diameter of approximately 1 mm. The preparation procedure of target material was as follows: 1) warm up the ethylene glycol in a thermal bath at 80°C, 2) mix $K_2Cr_2O_7$ of 40% by weight into ethylene glycol and magnetically stir the mixture for 10~15 minutes, 3) cool the mixture by immersing in cold water, 4) wait until precipitation is completed, and

fiter out the residue, 5) drop the solution down to liquid nitrogen through injection nozzles which were connected to a high voltage electrode. The high voltage ($\sim$2 KV) between the nozzles and the ground charged the drops up, and prevented them from sticking each other on a surface of liquid nitrogen before freezing.

Since the cryostat nose cone was set at an angle of 45° to the beam, the target was of edge-cut rhomboid form as is shown in Fig. 4. The edges of both sides were cut because the magnetic field was not uniform at these edges. The projection of the target transverse to the beam was 2.6 cm high $\times$ 3.6 cm wide. The target length averaged over the beam profile was 3.4 cm. The microwave cavity in which the target material was placed was a rectangular gold-plated copper box of 8.8 cm long, 2.6 cm high and 3.09 cm wide, as is shown in Fig. 4. Windows of 50 μm thick copper foil were provided on both sides of the cavity where the beam passed through. The top of the cavity was a fine wire mesh, through which liquid ^{3}He came in, and ^{3}He gas went out. The microwave was supplied into the target cavity through a 2 mm wide slit on the bottom plate of the cavity.

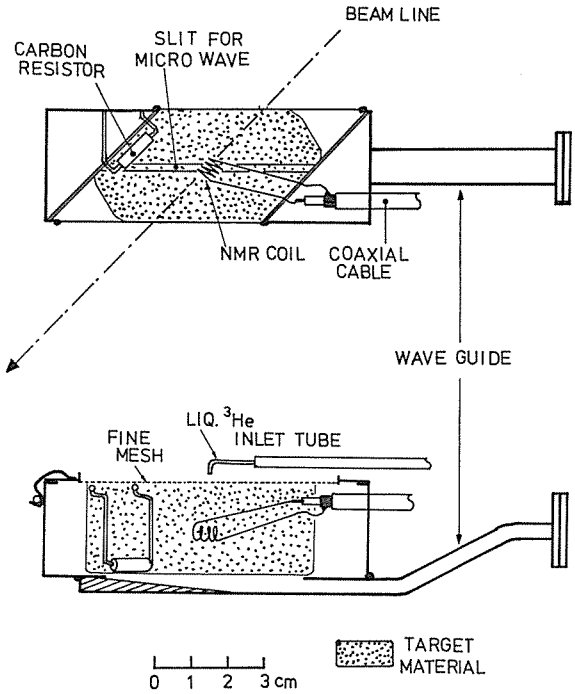

Fig. 4. A plan view and a side view of the polarized target cavity.

The measurement of the target polarization was accomplished by use of the nuclear magnetic resonance (NMR). A weak radio frequency magnetic field perpendicular to the polarizing magnetic field was applied to the target material near the resonant frequency (106 MHz) through a four-turn coil of 5 mm in diameter placed near the center of the target. Since protons aligned or anti-aligned with the polarizing magnetic field absorb or emit energies by transitions between these two spin states, the impedance of the radio frequency circuit changes while the frequency of the applied

radio frequency field changes. This impedance change integrated over ± 400 kHz around the resonant frequency was assumed to be proportional to the target polarization. The target polarization was calibrated by measuring the natural polarization at known temperature (about 0.7°K) without the microwave. The natural polarization P_0 was calculated from the Boltzmann factor for the populations of the two spin orientations. That is,

$$P_0 = \frac{1-\exp(-h\nu/kT)}{1+\exp(-h\nu/kT)} = \tanh(h\nu/2kT). \tag{12}$$

A calibrated carbon resistor and a McLeod gauge were used to measure the temperature T, while ν was the nuclear magnetic resonant frequency. h and k denote the Planck and Boltzmann constants, respectively. The measurement of P_0 was made prior to every experimental cycle. One cycle consisted of seven days, and a whole data set including runs for polarization up/down and carbon target at the same beam momentum were taken in the same cycle. The target polarization was reversed very several hours.

The NMR device was that of a super heterodyne type and had an analog compensator which cancelled smooth background signals. The details will be described elsewhere[15]. The OKITAC 4300 b computer was used to control the NMR device. A nine bit D–A converter was used to sweep the radio frequencies of the NMR signal, and the output signal was amplified and converted to a DC level in the NMR device. After the background was compensated, the signal was sent to a twelve bit A–D converter. Since the device was DC-coupled, a possible zero level drift was cancelled with another nine bit D–A converter. These NMR signals were averaged over ten sweeps in the computer, and further remaining background was subtracted by fitting the background at either side of the signal. The averaged NMR signal thus obtained was integrated by the computer and displayed on a scope as is shown in Fig. 5a and 5b. The value of target polarization was transmitted to the PDP 11/45 computer for every 17.5 seconds, and was also recorded on a pen recorder chart using an eight bit D–A conveter to monitor the shift of the target polarization. All the data communications were performed through a CAMAC system. The diagram of the system is shown in Fig. 6.

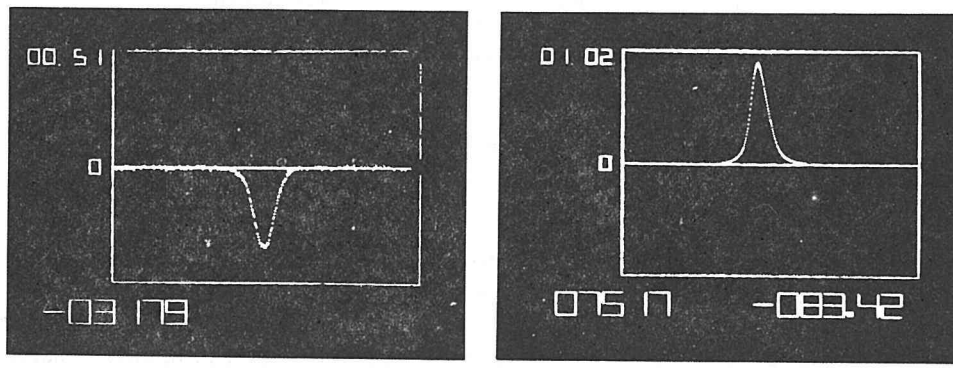

(a) (b)

Fig. 5a. The NMR signal for the natural polarization. (200-sweep)
Fig. 5b. The NMR signal for the dynamic polarization. (10–sweep)

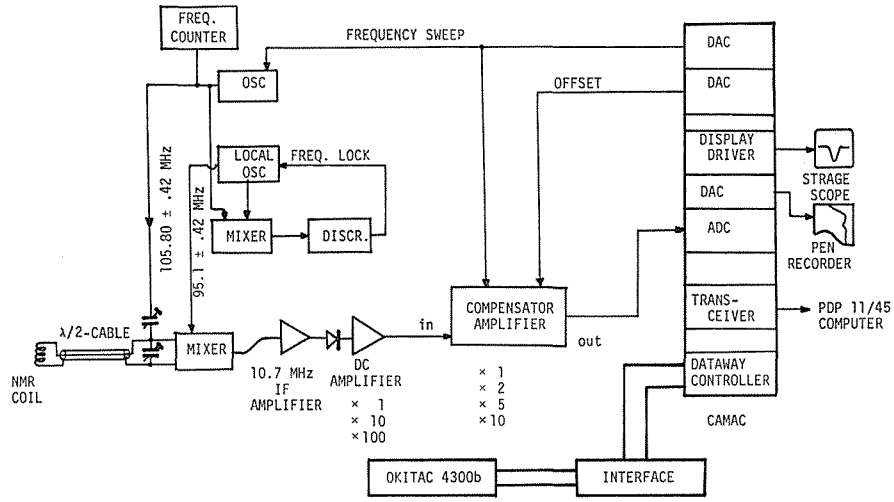

Fig. 6. The block diagram of the measuring system of the target polarization.

200 sweeps of the signals and the background base line curves were measured for the natural polarization. The background signals were obtained by slightly modifying the magnetic field off the resonance. Then the natural polarization was obtained by performing the same process mentioned above.

During one experimental cycle, the polarized target was cooled down for 4 to 5 days to collect the events with target polarizations up/down, and the rest of 1 or 2 days were consumed to measure the background events with the carbon target. The data were collected when the target polarization reached higher than 50%. The target was operated at about 0.5°K and the averaged polarization of 60~70% was achieved throughout the experiment.

D. Beam Counters and Veto Counters

The scintillation counters of the beam trigger system and the vetoing system for outgoing charged particles are shown in Fig. 2 and 7. The beam counters and the veto counters were about the same as those of the differential cross section measurement[13]. The beam was defined by the counter **S1**, 6×6 two dimensional hodoscope counter **1H**, the counter **S2**, and the veto counter **VB** which vetoed the beam halo out side of a 1.8 cm high and 2.5 cm wide hole. The hodoscope counter **1H** were used only as two single scintillation counters by summing signals from six horizontal and six vertical counters.

A 100 cm long gas Cherenkov counter of threshold type was placed between **S1** and **1H** to reduce electrons and muons contained in the pion beam. The Cherenkov lights emitted in freon 12 gas with pressures ranging from 0.8 to 2.0 atm were viewed by an RCA 8854 photomultiplier tube. A typical pressure curve measured by the gas Cherenkov counter is displayed in Fig. 8. The contamination of electrons and muons in the pion beam ranged from 2.2% (at 1.965 GeV/c) to 1.3% (at 2.960 GeV/c), and was reduced to be negligibly small during the experiment.

The veto counters **TVG1**, **TVG2**, **TVN1**, **TVN2**, **TVPT** and **TVPB** surrounded the target. The counters **TVG1** and **TVG2** detected charged particles leaving the target

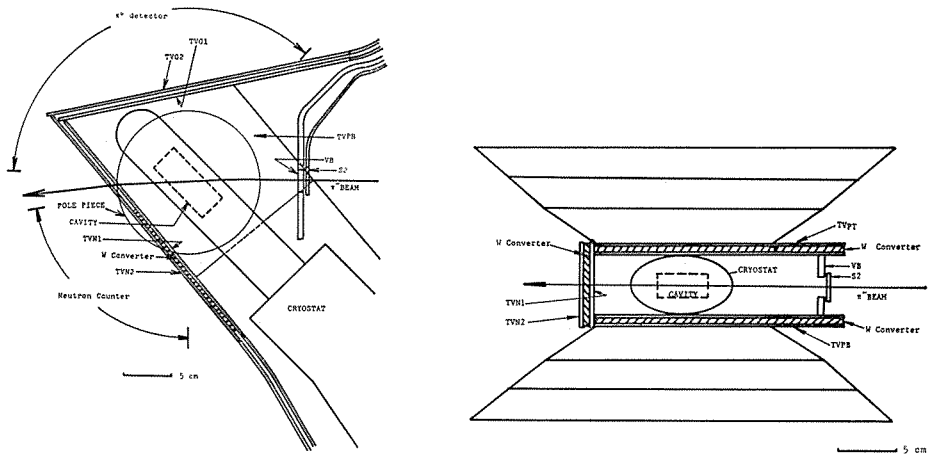

(a) (b)

Fig. 7a. A plan view of the veto counter assembly surrounding the target.
Fig. 7b. A side view of the veto counter assembly surrounding the target.

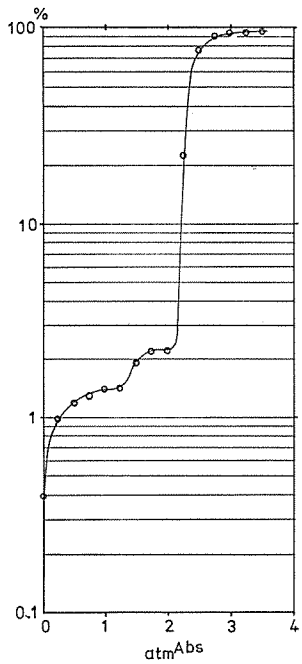

Fig. 8. A typical pressure curve measured with the gas Cherenkov counter of threshold type at 1.965 GeV/c. The solid curve is only for the eye-leading.

towards the π°-detection system, while the counters **TVN1** and **TVN2** towards the neutron counters. A tungsten sheet of 3 mm thick was placed between the counters **TVN1** and **TVN2** so as to detect γ-rays with the counter **TVN2**. The counters **TVPT** and **TVPB**, which also had tungsten sheets of 3 mm thick between two scintillators,

detected both charged particles and γ-rays leaving the target towards the magnet polefaces. The hole counter **VB** also detected charged particles scattered backward. All the counters mentioned above were viewed by RCA 8575 or HTV R329P photomultiplier tubes through rather long light pipes. These photomultiplier tubes were carefully shielded against the strong fringing magnetic flux from the magnet of the polarized target.

E. Lead Glass Counters

The lead glass counters were assembled in five boxes as matrices: the box #1 had six lines and five rows, while all other boxes had six lines and six rows. The radial and polar coordinates of the center of the face of each box with respect to the center of the target can be found in Table I.

Table I. The radial and polar coordinates of the lead glass counter array box. R denotes the distance between the center of the targe and the center of the front face of the box. θ is the polar angle of the box with respect to the incoming beam line, not to the actual "0° line". H denotes the vertical displacement of the box with respect to the horizontal plane of scattering. + and − mean that the box is above and below the medium horizontal plane, respectively.

BOX	R (cm)	θ (°)	H (cm)
#1 (6×5)	227.5	9.0	+0.2
#1 (6×6)	154.0	26.9	−0.2
#3 (6×6)	126.1	51.0	+0.3
#4 (6×6)	98.0	80.4	0.0
#5 (6×6)	77.3	118.1	0.0

Each lead glass counter consisted of an SF–6N lead glass block having a volume of $7.5 \times 7.5 \times 23.5$ cm^3 (14 radiation lengths) and was viewed by an HTV R329P photomultiplier tube.

A combination of 8 mm thick lead converter plate and four-layer wire spark chambers was placed in front of each box. The box #5 was placed nearest to the polarizing magnet. Therefore, the combination of the lead plate of 5 mm thick and iron plate of 9.6 mm thick was placed in front of the box. The iron plate shielded the leadglass counters from fringing field of the polarizing magnet. The wire spark chambers were used to measure the directions of γ-rays from the π^0 mesons. However, the informations from the wire spark chambers were used only for the test of the performance of the detection system because of its rather small detection efficiency for γ-rays.

As was mentioned in Section **II–D**, the charged particles emitted from the target towards these lead glass counters were detected with the veto **TVG1** and **TVG2** placed close to the target. However, the box #1 was set up very close to the incident beam line. Therefore, a pair of scintillation counters **GV1** and **GV2** were placed in front of the box #1 to obtain high rejection efficiency for the charged particles.

The bias levels for the lead glass counters were set at 200 MeV for the counters contained in the box #1 and #2, and at 100 MeV for those in the box #3, #4 and #5.

A more detailed description was given in Ref. 13.

F. Neutron Counters

The neutron counters were also assembled in five boxes, but the number of counters contained in each box was different from each other. The box #1 had six lines and three rows, #2 and #3 had six lines and five rows and #4 and #5 had four lines and five rows. The radial and polar coordinates of each box with respect to the center of the target are listed in Table II.

Each neutron counter consisted of a plastic scintillator having a volume of $10 \times 10 \times 30$ cm^3 and being viewed by an HTV R329P photomultiplier tube through a

Table II. The radial and polar coordinates of the neutron counter array box for incident momenta 1.965 and 2.960 GeV/c (a) and for 2.168, 2.360 and 2.566 GeV/c (b). Notations are the same as in Table I.

(a)

BOX	R (cm)	θ (°)	H (cm)
#1 (6×3)	479.2	12.0	0.0
#2 (6×5)	429.7	19.0	0.0
#3 (6×5)	296.3	28.0	+0.15
#4 (5×4)	159.2	43.0	+0.25
#5 (5×4)	81.3	71.0	+0.25

(b)

BOX	R (cm)	θ (°)	H (cm)
#1		not used	
#2 (6×5)	319.2	15.4	0.0
#3 (6×5)	296.3	28.0	+0.15
#4 (5×4)	159.2	43.0	+0.25
#5 (5×4)	81.3	71.1	+0.25

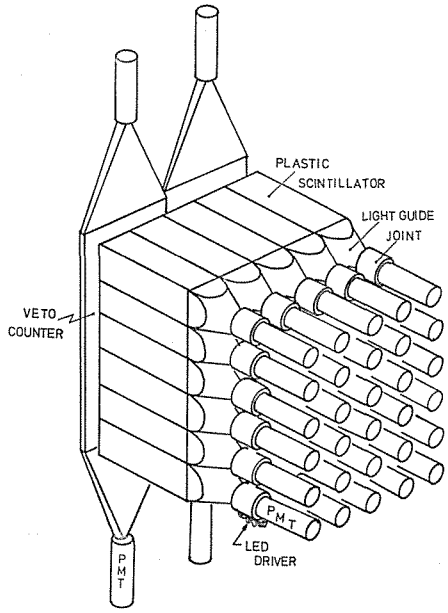

Fig. 9. A sketch of the neutron nounter array box with the veto counters.

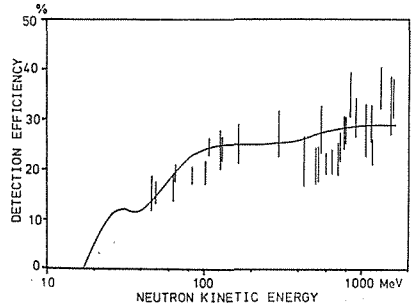

Fig. 10. The detection efficiency of the neutron counter as a function of the kinetic energy of neutron. The curve indicates the results of the Monte Carlo simulation.

lucite light guide. A sketch of the neutron counter box can be seen in Fig. 9.

Veto counters $\mathbf{NV}_i$ were placed in front of each neutron counter box for the protection against charged particles which were not detected with the veto counters surrounding the target (**TVN1** and **TVN2**). The size of the veto counter was 30×26 cm^2, and each box was covered by a pair of these veto counters.

All the neutron counters were exposed to the pion beam before the experiment so as to set the bias level. The bias level was chosen to be 20 MeV in terms of the proton energy.

The detection efficiency for neutrons was measured as a function of the kinetic energy of the neutron during the differential cross section measurement using $\pi^-p\to\pi^0n$ scattering. It was found to be 25% on an average, and agreed with the Monte Carlo simulation. A typical detection efficiency curve is shown in Fig. 10.[16]

The drift of the gains of these neutron counters were monitored by measuring the counting rates of each counter throughout the experiment.

G. Electronics and On-line Computer

The outline of the electronic system is shown in Fig. 11. In the beam flux counting system, if two beam particles arrived within less than 40 nsec, both signals were vetoed, and no pulses were generated from the coincidence unit of **DTF**. This protection against the "wild beam" was done by the counter **S1** as follows. The signal from **S1** was split into two channels. One was fed into an updating discriminator, and the other into a non-updating discriminator whose threshold levels and output pulse widths were the same to one another. The output pulse from the up-

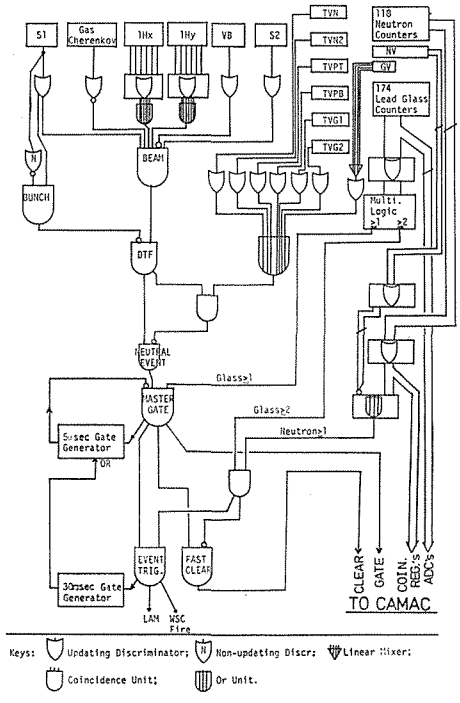

Fig. 11. The block diagram of the electronics.

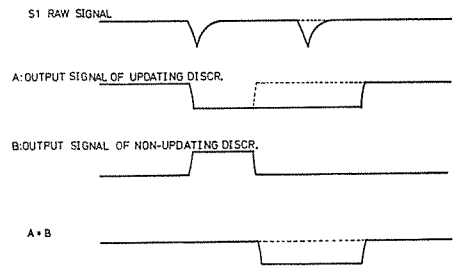

Fig. 12. An illustration of the protection circuit for the bunched beam with two successive beam signals.

dating discriminator and the inverted output pulse from the non-updating one was fed into the coincidence unit **BUNCH**. Since the non-updating discriminator does not produce output pulse for input pulse which arrived within the time of twice the output pulse width from the previous input pulse, while the updating one does, the coincidence unit **BUNCH** produces output pulse whenever the counter **S1** received two successive signals within a short time interval. Fig. 12 illustrates this feature schematically. Then, the **DTF** signal was vetoed with the summed signals of all the veto counters of **VB**, **TVG1**, **TVG2**, **TVN1**, **TVN2**, **TVPT**, **TVPB**, **GV1** and **GV2**. This signal was called as **NEUTRAL EVENT**. In order to reduce background events, it was required in the trigger condition that at least two lead glass counters were fired. This requirement was realized as follows. The **MASTER GATE** signals were generated when at least one lead glass counter was fired in coincidence with the signals **NEUTRAL EVENT**. That is,

$$\textbf{MASTER GATE} = \textbf{NEUTRAL EVENT} \cdot (\geqq 1 \text{ lead glass}). \qquad (13)$$

The **MASTER GATE** signal opened the gates of the A–D converters for the lead glass counters and of the parallel coincidence registers for the neutron counters and others, because they required rather fast gates. This **MASTER GATE** was not used for an interruption for the computer nor firing the wire spark chambers. As the final step, the logic signals **EVENT TRIG** or **FAST CLEAR** were generated according as at least one neutron counter and at least two lead glass counters were fired in coincidence with the **MASTER GATE** signal or not. These logics are

$$\textbf{EVENT TRIG} = \textbf{MASTERGATE} \cdot (\geqq 1 \text{ neutron}) \cdot (\geqq 2 \text{ lead glass}), \qquad (14)$$

$$\textbf{FAST CLEAR} = \textbf{MASTERGATE} \cdot \overline{(\geqq 1 \text{ neutron}) \cdot (\geqq 2 \text{ lead glass})}. \qquad (15)$$

Thus, the **EVENT TRIG** signals interrupted the computer and fired the wire spark chambers, and all the informations were stored into the PDP 11/45 computer. An inhibiting gate of 30 msec duration was generated to shut down whole the system during the event processing by the computer and the spark chamber recovery time. On the other hand, if the **FAST CLEAR** signal was generated, all of the A–D converters and the coincidence registers were reset, and an inhibiting gate of only 5 μsec duration was generated, whose duration was enough to reset the A–D converters and the coincidence registers. This rather complicated triggering system satisfied the strict requirements of fast gating for the A–D conveters and the coincidence registers.

Whenever the **EVENT TRIG** signal was produced, the PDP 11/45 computer was interrupted through a CAMAC LAM signal, and following informations were transferred into the computer via CAMAC system: 1) pulse heights of all the lead glass counters analyzed with the A–D converters; 2) bit pattern from all the neutron counters and the beam line hodoscope recorded on the parallel coincidence registers; 3) numbers of the **DTF** signals, the **BEAM** signals, etc. recorded with CAMAC blind scalers; 4) target polarization transmitted from the OKITAC 4300b computer through the transmitter/receiver modules; 5) informations of the wire spark chambers. The informations per event amounted to 432 words $\times$ 16 bits/word.

At the end of every beam spill, another interruption signal was generated, and the stored informations were transferred to the magnetic tape on this interruption, if a buffer for ten events was filled up.

During the run, the PDP 11/45 computer monitored the detection system by displaying histograms of the lead glass counters and the neutron counters and also

displaying two dimensional plots of the impact points of γ-rays on a CRT. At the end of the runs, contents of 32 six-digits 80 MHz visible scalers were read into the computer with CAMAC-scaler interface modules. Then, they were also recorded on the magnetic tape and printed out together with such summary histograms as mentioned above.

On the other hand, during the run, the same informations that were recorded on the magnetic tape were transmitted to the KEK central computer HITAC 8800 via on-line network KEKNET. The program then analyzed the informations, and returned back histograms for γ–γ invariant mass, γ–γ opening angle and reconstructed π°'s momentum distribution in the center of mass system (CMS) of $\pi^- p$.

The more detailed description about the on-line computer system is given in Ref. 13.

III. DATA Reduction

A. Event Processing

The number of the triggered events and the total flux of the incident pion beam used at each momentum were summarized in Table III together with the amount of consumed time.

Table III. The summary of the data.

Momentum	Target	Total Beam Flux	Triggered Events	Total Consumed Time
1.965 GeV/c	UP	17733×10^6	76844	34.2 hours
	DOWN	18951	82759	36.9
	CARBON	14452	45298	28.7
2.168	UP	17041	80587	26.0
	DOWN	17416	83427	28.5
	CARBON	12684	41919	18.7
2.360	UP	23846	124017	40.0
	DOWN	21505	115975	35.9
	CARBON	18860	75866	29.0
2.566	UP	21357	145836	41.4
	DOWN	20334	139001	38.9
	CARBON	16794	85848	30.6
2.960	UP	22031	99592	50.5
	DOWN	20078	91425	44.2
	CARBON	16878	57712	33.8

The data for both the polarized target and the carbon target were processed with the KEK central computer of HITAC 8800 as follows: 1) events having two separate showers were selected; 2) the invariant mass of the two γ-rays was calculated; 3) the opening angle between the two γ-rays in CMS was calculated; 4) three-momentum vectors of the scattered π° mesons were reconstructed; 5) the measured direction of the recoil neutron was compared with the prediction from the three-momentum victor of the π° meson using two-body kinematics; 6) the events were selected by making cuts on these quantities, and finally the polarization parameters were calculated from the event distribution in $\cos\theta^*$, where θ^* denotes the scattering angle of the π° meson in CMS.

1) The energy of the γ-ray was absorbed in the lead glass blocks by developing a cascade shower. Therefore, the energy of single γ-ray was deposited not only in the single lead glass block, but also deposited in adjacent blocks due to the finite lateral distribution of the cascade shower. On the other hand, the lead glass counters were set up so that two γ-rays from the π° mesons hit at least every other block of the lead glass counters. About 3/4 of collected events were found to be caused by single γ-ray which deposited the energy in adjacent few blocks. These events were rejected at the first step. The events associated with two energetic γ-rays were selected and amounted to be 25% of the collected events. The events having more than two energetic γ-rays were found to be less than 3% of the two-γ events.

2) The energy of each γ-ray was evaluated from the pulse height using the gain curve measured with the monochromatic electrons. The details of the energy calibration of the lead glass counters appear in Ref. 13. The energies of γ-ray depositted in adjacent blocks were also summed up in this process.

If a γ-ray hit the counter placed at the most outside of the lead glass counter array, the part of the cascade shower was missed away outside the lead glass block. Therefore, the fraction of the energy missed from the counter was also corrected taking account of the results of the energy calibration measurement mentioned above. Finally, the energy loss in the lead converter placed in front of the lead glass counters was corrected to evaluate the energy of the γ-ray.

The impact point of the γ-ray was assumed to be at the center of the face of the lead glass counter whose depositted energy was the largest among the adjacent lead glass counters. Then, the direction of the detected γ-ray was obtained as a line joining this impact point with the center of the target.

The invariant mass of these two γ-rays was calculated for each event by using thus measured energies and directions of two γ-rays. The distribution of the invariant mass was so clean, that only loose cuts were applied to select the events as are shown in Fig. 13. About 20% of all the collected events remained after this step.

3) The opening angle in CMS was also evaluated for the passed events. Again, loose cuts were applied with the same reason. As is shown in Fig. 14, the low cut was chosen below the minimum opening angle, while the high cut was applied at an angle below the minimum opening angle for η mesons.

4) The three-momentum vector of the mother π° was reconstructed from the measured energies and directions of the two γ-rays applying the kinematical constraints. The details of the procedure are described in Ref. 17.

5) The direction of the recoil neutron in the laboratory system (LAB) was then calculated from these three-momentum vector of the π° meson assuming two-body kinematics of the charge exchange scattring.

On the other hand, the measured direction of the neutron was evaluated from the line joining the target center with the center of the face of the neutron counter which was fired. For the events having more than one firing neutron counters, the measured neutron direction was chosen to be the one which was closer to the kinematical prediction. Typically, 60% of the two-γ events fired a single neutron counter, 20% fired two counters and 20% fired more than two counters.

Using the predicted angles θ_n°, ϕ_n° and the measured angles θ_n, ϕ_n of the recoil neutron, following quantities were calculated:

$$\Delta\phi/\sigma=(\phi_n-\phi_n^\circ)/\sigma \tag{16}$$

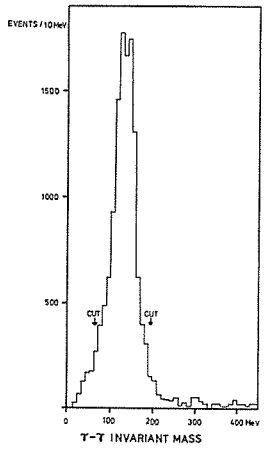

Fig. 13.

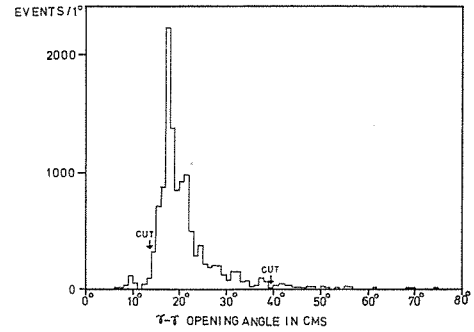

Fig. 14.

Fig. 13. An invariant mass distribution of two γ-rays at 2.168 GeV/c. The carbon target background is subtracted.

Fig. 14. A distribution of the opening angle in CMS between two γ-rays at 2.168 GeV/c. The carbon target background is subtracted.

$$\Delta\theta/\sigma=(\theta_n-\theta_n^\circ)/\sigma \tag{17}$$

$$\sigma=d/R, \tag{18}$$

where d is the dimension of the face of the neutron counter, that is 10 cm, and R is the distance between the target center and the center of the face of the neutron counter.

In order to reduce inelastic events and events from the bound protons, rather tight cuts were applied to the distributions of these quantities, $\Delta\phi/\sigma$ and $\Delta\theta/\sigma$. Typi-

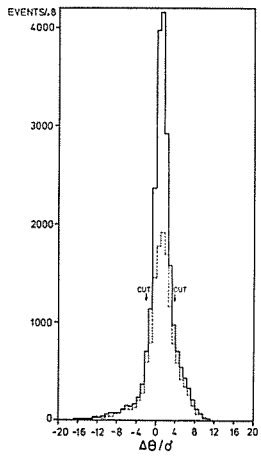

(a)

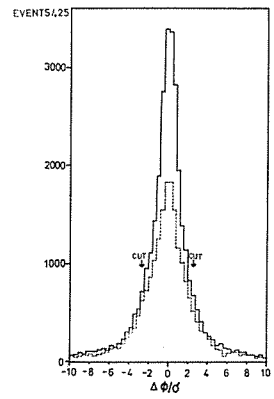

(b)

Fig. 15a. A $\Delta\phi/\sigma$ distribution at 2.168 GeV/c. The solid and dashed histograms indicate the distributions for the polarized target run and the carbon run, respectively.

Fig. 15b. A $\Delta\theta/\sigma$ distribution at 2.168 GeV/c. The solid and dashed histograms indicate the distributions for the polarized target run and the carbon run, respectively.

cally, the events were selected with the conditions $-2.2 \leqq \Delta\phi/\sigma \leqq 2.2$ and $-1.6 \leqq \Delta\theta/\sigma \leqq 3.2$ as are shown in Fig. 15a and 15b. About 12% of the collected events remained after this step.

6) Finally, the momenta of the π° mesons in CMS ($p^*_{\pi^\circ}$) were evaluated for the passed events. A typical momentum distribution is shown in Fig. 16. The events were selected if the evaluated $p^*_{\pi^\circ}$ lays between $75 \sim 80\%$ and $120 \sim 125\%$ of the value which was predicted from the kinematics for $\pi^- p \to \pi^\circ n$ scattering. Finally, $8 \sim 10\%$ out of all the collected events were selected.

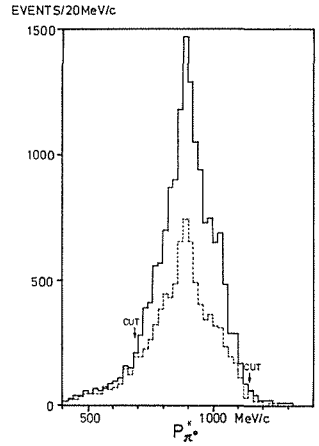

Fig. 16. A distribution of the π° momentum in CMS at 2.168 GeV/c. The solid and dashed histograms indicate the distributions for the polarized target run and the carbon target run, respectively.

B. Background Subtraction

The background events arising from the bound protons in heavy nuclei such as carbons in ethylene glycol and metals of the cavity and the cryostat wall were measured by replacing the beads of ethylene glycol by three layers of graphite plate in the cavity. (the carbon target run) These graphite plates contained the same amount of bound protons as the ethylene glycol. The volume of the ethylene glycol were measured for every experimental cycle and were constant within $\pm 3\%$. However, it was expected that the density of the ethylene glycol target might deviate from the expected one because of the non-uniformity of the shape of the ethylene glycol beads.

In order to clarify this uncertainty, independent test runs were executed at 2.168 GeV/c. A solid block of polyethylene of 6.00 cm long and a block of graphite of 2.82 cm long were used as targets instead of the polarized target. The length of the graphite block was so made to contain the same number of carbon atoms as the polyethylene block within an accuracy of 0.7%. From these test runs, the yields from free pritons were obtained as a function of $\cos\theta^*$. The results are shown in Fig. 17 together with the results obtained from the polarized target runs. These two distributions agreed with each other giving a value of 1.32 for χ^2 per data point. Moreover, the minimum of χ^2 was searched by changing the length of the graphite plates used for the carbon target run as a free parameter. Thus, it was found that the actual length of the graphite plates and the result of the χ^2 search differed only 2.2%.

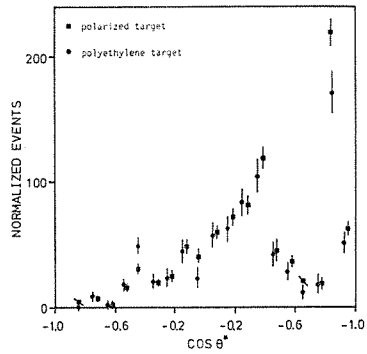

Fig. 17. The yields from free protons obtained from the polarized target run and from the polyethylene target run. The ordinate indicates the number of events per 10^9 incident pions and per 1 g/cm^2 of the free protons cantained in each target.

This difference is smaller than the uncertainty of 3% in the volume of the ethylene glycol mentioned above.

Finally, the background due to the inelastic events arising from such as the $\pi^-p\to\pi^\circ\pi^\circ n$ reaction was neglected, because it was found in the measurements of the differential cross sections using the hydrogen target[13] in which these events were rejected by the event selection with the angular correlation between the π° meson and neutron described in Section **III–A–(5)** of this paper.

IV. Results and Conclusions

A. Polarization Parameters

The angular resolutions of the detection system were evaluated with a Monte Carlo simulation. The angular resolutions in $\cos\theta^*$ at 1.965 and 2.960 GeV/c are shown in Fig. 18. The acceptance of the apparatus was also evaluated with the Monte Carlo simulation, and the acceptance at 2.168 GeV/c is shown in Fig. 19. The bin width of $\cos\theta^*$ was chosen to be ± 0.05 with an exception at $\cos\theta^*=0.925$ where the bin width is ± 0.025.

The polarization parameters were calculated by use of the formula (10) from the

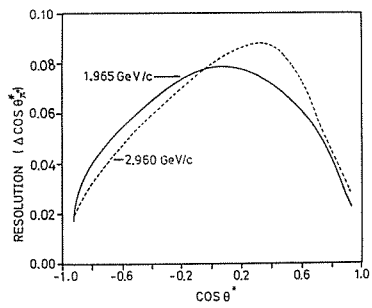

Fig. 18.

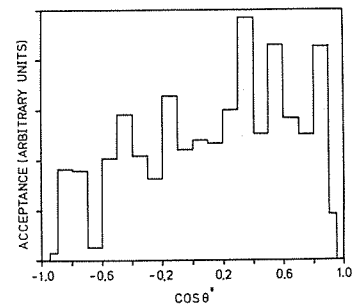

Fig. 19.

Fig. 18. The angular resolution in $\cos\theta^*$ defined as full width at half the maximum.
Fig. 19. The acceptance of the apparatus as a function of $\cos\theta^*$ at 2.168 GeV/c.

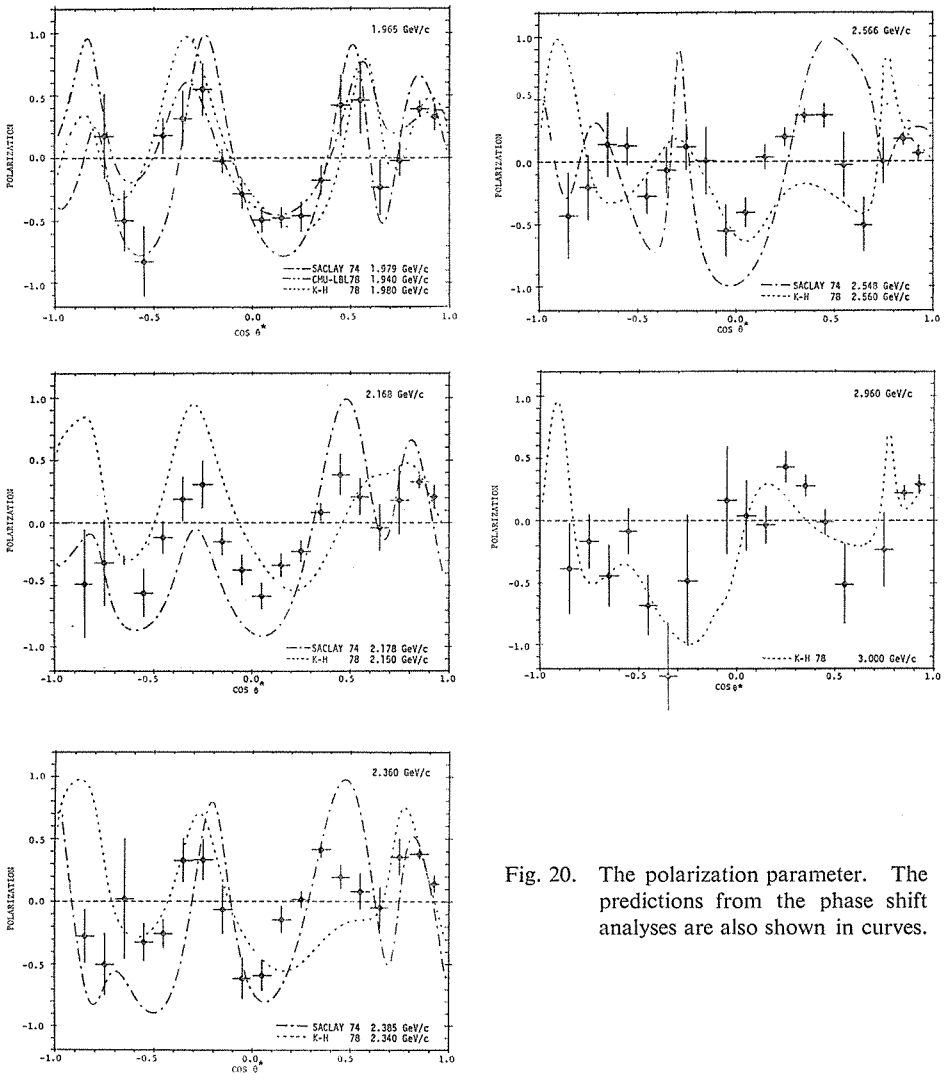

Fig. 20. The polarization parameter. The predictions from the phase shift analyses are also shown in curves.

Table IV. The systematic errors.

Systematic Error Source	1.965 GeV/c	2.168 GeV/c	2.360 GeV/c	2.566 GeV/c	2.960 GeV/c
Temperature Measurement	3%	2%	2%	1%	3%
Natural Pol. Signal	5%	4%	4%	3%	5%
Background Subtraction	3%	3%	3%	3%	3%
Overall Relative Systematic Error	1 ± 0.07	1 ± 0.05	1 ± 0.05	1 ± 0.04	1 ± 0.07

Table V. Polarization parameters for $\pi^- p \to \pi^0 n$ scattering. Errors are statistical only.

$\cos\theta^*_{\pi^0}$	Polarization Parameters				
	p_{LAB}=1.965 GeV/c $\sqrt{s}$=2.144 GeV	p_{LAB}=2.168 GeV/c $\sqrt{s}$=2.231 GeV	p_{LAB}=2.360 GeV/c $\sqrt{s}$=2.310 GeV	p_{LAB}=2.566 GeV/c $\sqrt{s}$=2.392 GeV	p_{LAB}=2.960 GeV/c $\sqrt{s}$=2.542 GeV
−0.85 ±0.05	— —	−0.49±0.44	−0.28±0.21	−0.43±0.35	−0.38±0.36
−0.75 ±0.05	0.17±0.34	−0.32±0.34	−0.50±0.25	−0.20±0.26	−0.17±0.22
−0.65 ±0.05	−0.50±0.24	— —	0.02±0.48	0.14±0.26	−0.44±0.25
−0.55 ±0.05	−0.83±0.29	−0.56±0.19	−0.32±0.15	0.13±0.15	−0.08±0.19
−0.45 ±0.05	0.18±0.14	−0.12±0.13	−0.26±0.11	−0.27±0.14	−0.68±0.24
−0.35 ±0.05	0.32±0.22	0.19±0.17	0.33±0.18	−0.07±0.18	−1.26±0.45
−0.25 ±0.05	0.55±0.21	0.30±0.19	0.33±0.16	0.12±0.18	−0.48±0.53
−0.15 ±0.05	−0.02±0.10	−0.15±0.11	−0.06±0.19	0.01±0.27	— —
−0.05 ±0.05	−0.28±0.12	−0.37±0.12	−0.61±0.17	−0.55±0.21	0.16±0.43
0.05 ±0.05	−0.49±0.10	−0.58±0.10	−0.59±0.12	−0.40±0.12	0.04±0.28
0.15 ±0.05	−0.47±0.08	−0.34±0.09	−0.14±0.11	0.04±0.10	−0.03±0.15
0.25 ±0.05	−0.46±0.11	−0.22±0.09	0.02±0.07	0.20±0.07	0.43±0.12
0.35 ±0.05	−0.18±0.12	0.08±0.07	0.41±0.07	0.37±0.06	0.28±0.09
0.45 ±0.05	0.42±0.25	0.38±0.16	0.19±0.10	0.37±0.10	−0.01±0.10
0.55 ±0.05	0.46±0.26	0.21±0.14	0.08±0.15	−0.03±0.26	−0.51±0.32
0.65 ±0.05	−0.23±0.22	−0.04±0.19	−0.05±0.16	−0.50±0.23	— —
0.75 ±0.05	−0.02±0.12	0.18±0.27	0.36±0.15	0.00±0.19	−0.23±0.30
0.85 ±0.05	0.39±0.07	0.33±0.05	0.38±0.04	0.18±0.04	0.22±0.06
0.925±0.025	0.33±0.11	0.21±0.09	0.14±0.07	0.07±0.06	0.29±0.08

$\cos\theta^*$ distributions for the selected events for the polarized target runs with target polarizations up and down and for the carbon target runs. The polarization parameters at some bins were omitted because of poor statistics due to small acceptances.

The final results are given in Table V and in Fig. 20. The errors given in the table are statistical only. A summary of the systematic errors are tabulated in Table IV.

Errors in evaluating the target polarization were the main part of the systematic errors. It arises from uncertainties in the temperature measurement in the evaluation of the natural polarization and uncertainties in the measurement of the natural polarization signals. The uncertainties in the temperature measurement were estimated from the discrepancies between the evaluated temperatures from the pressure measurement with the McLeod gauge and from the standard carbon resistor.

Another systematic error was that due to the uncertainty in the volume of the ethylene glycol. This error of 3% could introduce a systematic error of about 3% on the polarization parameter, since the background events were about the same amount as the free proton events.

The general feature of the polarization parameters is characterized by the steep oscillation in $\cos\theta^*$ with many nodes. The shape of oscillation varies as the incident momentum increases, especially at high momenta. It seems that this feature implies the effect of large angular momentum waves interfering with each other. In the forward region, two peaks having positive polarizations are seen at $\cos\theta^*=0.9$ and $0.4\sim0.5$ at all momenta. The second peak at $\cos\theta^*=0.4\sim0.5$ moves backwards and increases the with as the incident momentum increases. There is a region of negative polarization at around $\cos\theta^*=0.1$. The position of the bottom moves backwards slighly, and the width of the region becomes narrower as the incident momentum increases.

The polarization parameters were also evaluated for the parts of events rejected by the selection due to the direction of the recoil neutrons (Section **III–A–(5)**). The results are shown in Fig. 21, and proved that there are no systematic biases in the present measurement and the procedure of the data selection, which affects to the polarization parameters.

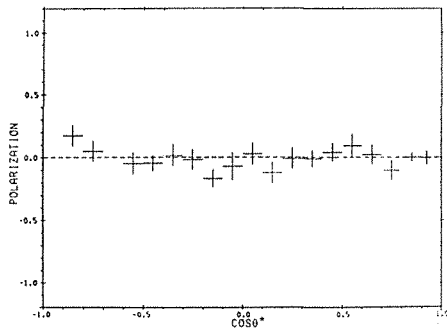

Fig. 21. The polarization parameter evaluated with the rejected events.

B. Comparison with Other Experiments

There are only two measurements on the $\pi^-p\to\pi^\circ n$ polarization parameter which have overlapping regions with our experiment.

The one is the experiment by Brown et al.[12] Their data extends over most of the angular range at 22 momenta. The data at the highest three momenta (1.975, 2.055 and 2.267 GeV/c) overlap with our region. Their results at 1.975 GeV/c are compared with our data at 1.965 GeV/c in Fig. 22. The results are in good agreement except in the range of $\cos\theta^*$ from -0.35 to -0.55.

The other is by Drobnis et al[5]. Their data are only at the forward angular range at nine momenta. The data at the lowerst three momenta (2.07 GeV/c, 2.50 GeV/c and 2.72 GeV/c) overlap with our region. Their results at 2.07 and 2.50 GeV/c are also compared with our results at 1.965 and 2.566 GeV/c, respectively in Fig. 23. The results are considered to be consistent although there are some small discrepancies. One should take into account that they used inorganic material as a polarized target (LMN target) in which only small fraction of free protons were contained.

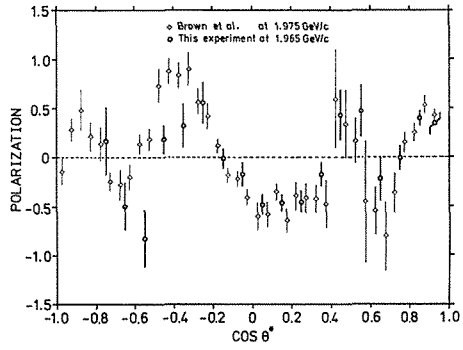

Fig. 22. A comparison of the present data with the data of Brown et al.[12]

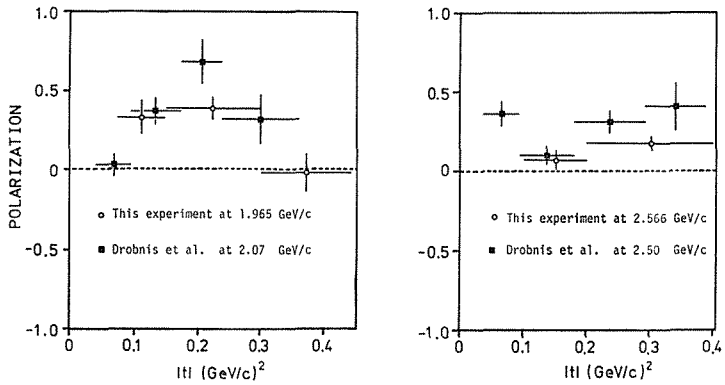

Fig. 23. A comparison of the present data with the data of Drobnis et al[5].

C. Comparison with a Regge Pole Model

Regge pole models have played a valuable role to describe high-energy scatterings. While the forward $\pi^{\pm}p$ elastic scattering can be described with the isospin 0 and 1 exchange in the t-channel, the charge exchange scattering is considered to be described only with the isospin 1 exchange. However, the naive Regge pole model, in which only ρ is exchanged for the charge exchange scattering, could not explain the non-zero

forward polarization parameters found at high energies, since any single Regge pole gives zero polariazation.

Barger and Phillips analyzed πN scattering amplitudes[18], through the range $0 \leqq -t \leqq 2$ (GeV/c)^2, in terms of P, P', P'', ρ and ρ' Regge poles using scattering data above about 5 GeV/c. They adopted ρ and ρ' Regge poles to describe the charge exchange scattering.

The polarization data by Bonamy et al. at 4.9 and 7.85 GeV/c[6] were consistent with the prediction of this model, while those by D. Hill et al. at 3.5 and 5.0 GeV/c[6] were not.

The present results are compared with their predictions in Fig. 24. The results on the differential cross section from Ref. 13 are also compared with them in the same figure. It exhibits clearly large discrepancies on the polarization parameter, while rather good agreements are obtained in the case of the differential cross section up to $t=-1.6$ (GeV/c)^2 The analysis well reproduces the forward peak and the dip at around $t=-0.5$ (GeV/c)^2 for the differential cross section. On the contrary, the prediction of the polarization parameter leads to only positive polarization and shows a bump at around $t=-0.5$ (GeV/c)^2 giving a large polarization and different behaviors from the present results even at 2.960 GeV/c. Further complicated mechanisms, which cannot be implied by the behaviors of the differential cross sections, are necessary to explain the polarization parameter of the charge exchange scattering in terms of the Regge pole models. Moreover, this indicates that the effects of the s-channel resonances seem to be important even at forward angles in the present energy region.

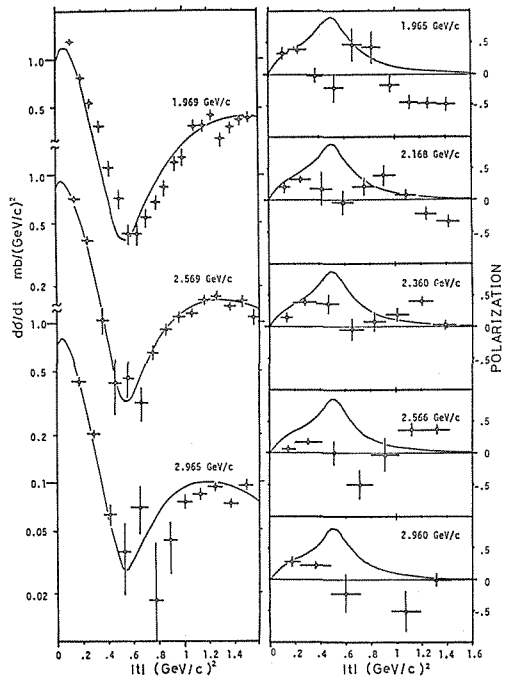

Fig. 24. A comparison of the present results with the prediction from the Regge pole model[18] (solid curve).

D. Comparison with Phase Shift Solutions

The results are also compared with the predictions from three kinds of phase shift analyses in Fig. 20: the SACLAY 74 phase shift solution by Ayed and Bareyre,[2] the CMU–LBL 78 solution by Cutkosky et al.[3] and the Karlsruhe-Helsinki 78 solution by Höller et al.[4] Since the SACLAY 74 analysis has solutions only up to 2.773 GeV/c, the predictions are compared with the results at lower four momenta. Similarly, the CMU–LBL 78 analysis has solutions up to 1.995 GeV/c, so only the preciction at 1.940 GeV/c is compared with the result at 1.965 GeV/c.

The χ^2's per datum point between each predictions and the results are tabulated in Table VI. These predictions are in general in poor agreements with the data except at 1.965 GeV/c. Since a rather small χ^2 of 2.46 at 2.960 GeV/c is considered to come from large errors in the result, it cannot be said that the agreement is good.

At 1.965 GeV/c, the predictions of the CMU–LBL 78 and the Karlsruhe-Helsinki 78 solutions equally agree with the data. The agreement is somewhat bad in the case of the SACLAY 74 predictions at this momentum. However, it should be pointed out that the new data on differential cross sections and polarization parameters for the charge exchange scattering of Brown et al. are not included in the SACLAY 74 analysis.

Table VI. The reduced χ^2's for the results and the predictions from three phase shift solutions.

Momentum	SACLAY 74	Karsruhe-Helsinki 78	CMU–LBL 78
1.965 GeV/c	5.48	2.49	1.36
2.168 GeV/c	8.81	8.14	—
2.360 GeV/c	10.86	13.94	—
2.566 GeV/c	12.06	12.51	—
2.960 GeV/c	—	2.46	—

At higher four momenta, the agreements are poor with the predictions of both the SACLAY 74 and the Karlsruhe-Helsinki 78 solutions although the latter used the data of Brown et al. up to 2.724 GeV/c for the differential cross sections and up to 2.267 GeV/c for the polarization parameters.

In order to see the effect of the present results on the phase shift solutions to some extent, we made Legendre expansions for the present results.

E. Legendre Polynomial Expansion

The differential cross section and polarization parameter for spin $0+\frac{1}{2}\to 0+\frac{1}{2}$ scattering can be parametrized in terms of the Legendre coefficients as follws;

$$d\sigma/d\Omega = q^{-2}\sum_n A_n P_n(\cos\theta^*), \tag{19}$$

$$P\cdot d\sigma/d\Omega = q^{-2}\sum_n B_n P'_n(\cos\theta^*)\cdot\sin\theta^*, \tag{20}$$

where q is the momentum of the incident beam in CMS. Since f and g in Equation (4) can be expressed in terms of the partial wave amplitudes T_{jl} as,

$$f = q^{-1}\sum_l [(l+1)T_{j=l+1/2,l} + lT_{j=l-1/2,l}]\cdot P_l(\cos\theta^*), \tag{21}$$

$$g=q^{-1}\sum_{l}(T_{j=l+1/2,l}-T_{j=l-1/2,l})\cdot P_l'(\cos\theta^*)\cdot\sin\theta^*, \tag{22}$$

the coefficients A_n and B_n can be expressed as the bilinear functions of the partial wave amplitudes. Simple expressions for the coefficients A_n and B_n in terms of any number of partial wave amplitudes are presented in Ref. 19 as follows;

$$A_n=2(2n+1)\sum_{j,j'}\frac{\kappa(j+j'-n)\kappa(j-j'+n)\kappa(-j+j'+n)}{\kappa(j+j'+n+1)} \times\begin{cases}(T_{j+}T^*_{j'+}+T_{j-}T^*_{j'-}) & \text{for } j+j'+n=\text{odd}\\ (T_{j-}T^*_{j'+}+T_{j+}T^*_{j'-}) & \text{for } j+j'+n=\text{even},\end{cases} \tag{23}$$

$$B_n=\frac{2(2n+1)}{n(n+1)}\sum_{j,j'}\frac{\kappa(j+j'-n)\kappa(j-j'+n)\kappa(-j+j'+n)}{\kappa(j+j'+n+1)} \times\begin{cases}(j'-j)\,\mathrm{Im}\,(T_{j-}T^*_{j'-}-T_{j+}T^*_{j'+}) & \text{for } j+j'+n=\text{odd}\\ (j+j'+1)\,\mathrm{Im}\,(T_{j+}T^*_{j'-}-T_{j-}T^*_{j'+}) & \text{for } j+j'+n=\text{even},\end{cases} \tag{24}$$

with $T_{j\pm}\equiv T_{j,l=j\pm1/2}$,
where $\kappa(\nu)$ is a function defined as,

$$\begin{aligned}&\kappa(\ 2n\ )=(2n)!/(n!)^2,\\ &\kappa(2n+1)=(2n+1)\kappa(2n),\\ &\kappa(\ n\ )=0 \quad \text{for} \quad n<0.\end{aligned} \tag{25}$$

The summation runs over the region $|j-j'|\leqq n\leqq j+j'$.

The decomposition of B_n up to $j=15/2$ is tabulated in Table VII. The left-hand column of the table is to be read as, for example,

$$\text{S1 P3} - \text{P1 D3} \longrightarrow \mathrm{Im}\,(S_1^*\cdot P_3-P_1^*\cdot D_3). \tag{26}$$

The weights of these combinations in the coefficient B_n are listed in the corresponding numerical entries.

The coefficients B_n's were calculated from the present results using a method of the least squares. The coefficients B_n were evaluated as dimensionless quantities using a unit of $\hbar=c=1$. The order of the polynomial to fit the data was tested by the reduced chi-squared χ^2_ν as a function of the order. At 1.965 GeV/c, the χ^2_ν becomes constant above the order of $N=9$, and at 2.168 and 2.360 GeV/c, $N=10$. At the high momenta of 2.566 and 2.960 GeV/c, $N=12$ was necessary to make the χ^2_ν's small enough. However, $N=12$ was chosen for the evaluation of B_n even at the low momenta in order to compare these coefficients with those of the Karlsruhe-Helsinki 78 solution[20]. At the low momenta, the coefficients evaluated by the expansions of order 9 or 10 almost coincided with those by order 12.

Because the data region is limited between $\cos\theta^*=-0.90$ and 0.95, the expansion showed unstable behavior to the coefficients B_n, especially at large n. In order to avoid this feature, some constraints should be added to the data at the forward and backward angle. The quantities,

$$\lim_{\substack{\theta^*\to 0^\circ\\ 180^\circ}}\frac{P\cdot \mathrm{d}\sigma/\mathrm{d}\Omega}{\sin\theta^*}=q^{-2}\sum_n B_nP'(\pm1), \tag{27}$$

were calculated using the Karlsruhe-Helsinki 78 solution, and they were added to the

data set for the expansion with a rather large error of $\pm 30\%$. In order to test whether these constraints mislead the resultant coefficients B_n or not, the same quantities calculated from the SACLAY 74 solution were also added with the same errors instead of those from the Karlsruhe-Helsinki 78 solution. It was found that the coefficients with these two kinds of constraints almost coincided with each other within the errors. The values of the differential cross sections on the left-hand side of Equation (20) were calculated by using the Legendre coefficients A_n given in Ref. 13.

Thus obtained B_n's are listed in Table VIII together with the diagonal errors and the χ^2_ν of the fits. The coefficients are also plotted in Fig. 25 together with those obtained by Höller et al[20]. from the data by Brown et al[12]. and also those obtained from the phase shift solutions of the Karlsruhe-Helsinki 78 and the SACLAY 74. The results obtained from the data of Brown et al. and those from the present data agree with each other except the coefficients B_1, B_2 and B_3. The coefficients at each momentum were compared with those from these two phase shift analyses at the momentum nearest to that of the data. The value of χ^2 for each coefficient is listed in Table IX. The χ^2's for the Karlsruhe-Helsinki 78 solution are small for almost all the coefficients at 1.965 GeV/c except for B_4 and B_9. At 2.168, 2.360 and 2.566 GeV/c, rather large values of χ^2 were obtained for B_1, B_2, B_3, B_5, B_6 and B_7.

In order to understand these features somewhat qualitatively in terms of the partial wave amplitudes, it will be necessary to know how each partial wave amplitude affects to the coefficients B_n. Although the weights of contributions of the partial waves on the coefficient B_n are listed in Table VII, It is not so useful in the present case, because they are expressed in terms of the product of two different partial waves, say T_{jl} and $T_{j'l'}$. For instance, if the amplitude $T_{j'l'}$ itself is small, a contribution of T_{jl} to a certain coefficient B_n is small even if a large weight appears in the corresponding entry in the Table VII. Therefore, in order to see the contribution of each partial wave amplitude directly, we calculated values of the derivatives of B_n with respect to the real and imaginary part of each partial wave amplitude by using the Karlsruhe-Helsinki 78 solution at each momentum p, as follows;

$$\frac{\partial \beta_n}{\partial \mathrm{Re}\,(T_{jl})}\Big|_{\substack{\mathrm{K-H78}\\ p_{LAB}=p}} \quad \text{and} \quad \frac{\partial B_n}{\partial \mathrm{Im}\,(T_{jl})}\Big|_{\substack{\mathrm{K-H78}\\ p_{LAB}=p}},$$

Since B_n is the bilinear function of the partial wave amplitudes, as is shown in Equation (24), these derivatives themselves are the actual weights of the contributions of the real and imaginary parts of the partial wave amplitudes for B_n.

These derivatives at 1.965 and 2.360 GeV/c are shown in Fig. 26a and 26b, respectively, together with the differences of Legendre coefficients,

$$\Delta B_n \equiv B_n^{mes} - B_n^{K-H}, \tag{28}$$

where B_n^{mes} is the Legendre coefficient obtained from the present data, and B_n^{K-H} is that from the Karlsruhe-Helsinki 78 solution at the momentum nearest to the corresponding momentum of the data, say, 1.980 and 2.340 GeV/c.

In the momentum region of the present experiment, the large angular momentum waves, such as G_7, G_9, H_{11} and I_{11} start to play important roles as are shown in Fig. 1. Moreover, the low angular momentum waves contribute to the coefficients B_n with small weights compared with those for the large angular momentum waves as is seen in Table VII. Therefore, only the derivatives with respect to the large angular momentum waves, such as G's, H's and I's, are shown in the figures.

Table VII.

	B(1)	B(2)	B(3)	B(4)	B(5)	B(6)	B(7)	B(8)	B(9)	B(10)	B(11)	B(12)	B(13)	B(14)	B(15)
SI P1	2.00	·	·	·	·	·	·	·	·	·	·	·	·	·	·
S 1 P 3 – P 1 D 3	−2.00	·	·	·	·	·	·	·	·	·	·	·	·	·	·
S 1 D 3 – P 1 P 3	·	2.00	·	·	·	·	·	·	·	·	·	·	·	·	·
S 1 D 5 – P 1 F 5	·	−2.00	·	·	·	·	·	·	·	·	·	·	·	·	·
S 1 F 5 – P 1 D 5	·	·	2.00	·	·	·	·	·	·	·	·	·	·	·	·
S 1 F 7 – P 1 G 7	·	·	−2.00	·	·	·	·	·	·	·	·	·	·	·	·
S 1 G 7 – P 1 F 7	·	·	·	2.00	·	·	·	·	·	·	·	·	·	·	·
S 1 G 9 – P 1 H 9	·	·	·	−2.00	·	·	·	·	·	·	·	·	·	·	·
S 1 H 9 – P 1 G 9	·	·	·	·	2.00	·	·	·	·	·	·	·	·	·	·
S 1 H11 – P 1 I11	·	·	·	·	−2.00	·	·	·	·	·	·	·	·	·	·
S 1 I11 – P 1 H11	·	·	·	·	·	2.00	·	·	·	·	·	·	·	·	·
S 1 I13 – P 1 K13	·	·	·	·	·	−2.00	·	·	·	·	·	·	·	·	·
S 1 K13 – P 1 I13	·	·	·	·	·	·	2.00	·	·	·	·	·	·	·	·
S 1 K15 – P 1 L15	·	·	·	·	·	·	−2.00	·	·	·	·	·	·	·	·
S 1 L15 – P 1 K15	·	·	·	·	·	·	·	2.00	·	·	·	·	·	·	·
P3 D3	1.60	·	2.40	·	·	·	·	·	·	·	·	·	·	·	·
P 3 D 5 – D 3 F 5	−3.60	·	−0.40	·	·	·	·	·	·	·	·	·	·	·	·
P 3 F 5 – D 3 D 5	·	1.43	·	2.57	·	·	·	·	·	·	·	·	·	·	·
P 3 F 7 – D 3 G 7	·	−3.43	·	−0.57	·	·	·	·	·	·	·	·	·	·	·
P 3 G 7 – D 3 F 7	·	·	1.33	·	2.67	·	·	·	·	·	·	·	·	·	·
P 3 G 9 – D 3 H 9	·	·	−3.33	·	−0.67	·	·	·	·	·	·	·	·	·	·
P 3 H 9 – D 3 G 9	·	·	·	1.27	·	2.73	·	·	·	·	·	·	·	·	·
P 3 H11 – D 3 I11	·	·	·	−3.27	·	−0.73	·	·	·	·	·	·	·	·	·
P 3 I11 – D 3 H11	·	·	·	·	1.23	·	2.77	·	·	·	·	·	·	·	·
P 3 I13 – D 3 K13	·	·	·	·	−3.23	·	−0.77	·	·	·	·	·	·	·	·
P 3 K13 – D 3 I13	·	·	·	·	·	1.20	·	2.80	·	·	·	·	·	·	·
P 3 K15 – D 3 L15	·	·	·	·	·	−3.20	·	−0.80	·	·	·	·	·	·	·
P 3 L15 – D 3 K15	·	·	·	·	·	·	1.18	·	2.82	·	·	·	·	·	·
D5 F5	1.54	·	1.60	·	2.86	·	·	·	·	·	·	·	·	·	·
D 5 F 7 – F 5 G 7	−5.14	·	−0.67	·	−0.19	·	·	·	·	·	·	·	·	·	·
D 5 G 7 – F 5 F 7	·	1.33	·	1.64	·	3.03	·	·	·	·	·	·	·	·	·
D 5 G 9 – F 5 H 9	·	−4.76	·	−0.94	·	−0.30	·	·	·	·	·	·	·	·	·
D 5 H 9 – F 5 G 9	·	·	1.21	·	1.64	·	3.15	·	·	·	·	·	·	·	·

D 5 H11 – F 5 I11	·	·	−4.55	·	−1.08	·	−0.38	·	·	·	·	·	·	·	·
D 5 I11 – F 5 H11	·	·	·	1.13	·	1.64	·	3.23	·	·	·	·	·	·	·
D 5 I13 – F 5 K13	·	·	·	−4.41	·	−1.16	·	−0.43	·	·	·	·	·	·	·
D 5 K13 – F 5 I13	·	·	·	·	1.08	·	1.63	·	3.29	·	·	·	·	·	·
D 5 K15 – F 5 L15	·	·	·	·	−4.31	·	−1.22	·	−0.47	·	·	·	·	·	·
D 5 L15 – F 5 K15	·	·	·	·	·	1.04	·	1.62	·	3.34	·	·	·	·	·
F7 G7	1.52	·	1.45	·	1.76	·	3.26	·	·	·	·	·	·	·	·
F 7 G 9 – G 7 H 9	−6.67	·	−0.91	·	−0.31	·	−0.12	·	·	·	·	·	·	·	·
F 7 H 9 – G 7 G 9	·	1.30	·	1.46	·	1.82	·	3.43	·	·	·	·	·	·	·
F 7 H11 – G 7 I 11	·	−6.06	·	−1.26	·	−0.48	·	−0.20	·	·	·	·	·	·	·
F 7 I11 – G 7 H11	·	·	1.17	·	1.44	·	1.85	·	3.55	·	·	·	·	·	·
F 7 I13 – G 7 K13	·	·	−5.71	·	−1.44	·	−0.60	·	−0.25	·	·	·	·	·	·
F 7 K13 – G 7 I13	·	·	·	1.08	·	1.41	·	1.87	·	3.64	·	·	·	·	·
F 7 K15 – G 7 L15	·	·	·	−5.48	·	−1.54	·	−0.68	·	−0.30	·	·	·	·	·
F 7 L15 – G 7 K15	·	·	·	·	1.01	·	1.39	·	1.88	·	3.72	·	·	·	·
G9 H9	1.52	·	1.40	·	1.54	·	1.92	·	3.63	·	·	·	·	·	·
G 9 H11 – H 9 I11	−8.18	·	−1.14	·	−0.41	·	−0.19	·	−0.08	·	·	·	·	·	·
G 9 I11 – H 9 H11	·	1.28	·	1.38	·	1.57	·	1.98	·	3.78	·	·	·	·	·
G 9 I13 – H 9 K13	·	−7.34	·	−1.57	·	−0.64	·	−0.31	·	−0.14	·	·	·	·	·
G 9 K13 – H 9 I13	·	·	1.14	·	1.35	·	1.58	·	2.03	·	3.90	·	·	·	·
G 9 K15 – H 9 L15	·	·	−6.85	·	−1.77	·	−0.79	·	−0.40	·	−0.19	·	·	·	·
G 9 L15 – H 9 K15	·	·	·	1.05	·	1.32	·	1.58	·	2.06	·	4.00	·	·	·
H11 I11	1.51	·	1.37	·	1.45	·	1.64	·	2.07	·	3.96	·	·	·	·
H11 I13 – I11 K13	−9.69	·	−1.37	·	−0.51	·	−0.24	·	−0.13	·	−0.06	·	·	·	·
H11 K13 – I11 I13	·	1.27	·	1.35	·	1.46	·	1.67	·	2.14	·	4.10	·	·	·
H11 K15 – I11 L15	·	−8.62	·	−1.87	·	−0.79	·	−0.40	·	−0.22	·	−0.11	·	·	·
H11 L15 – I11 K15	·	·	1.13	·	1.31	·	1.46	·	1.70	·	2.18	·	4.22	·	·
I13 K13	1.51	·	1.35	·	1.40	·	1.52	·	1.74	·	2.22	·	4.27	·	·
I13 K15 – K13 L15	−11.20	·	−1.60	·	−0.60	·	−0.30	·	−0.17	·	−0.09	·	−0.05	·	·
I13 L15 – K13 K15	·	1.27	·	1.33	·	1.41	·	1.54	·	1.78	·	2.28	·	4.40	·
K15 L15	1.51	·	1.34	·	1.37	·	1.45	·	1.59	·	1.83	·	2.36	·	4.56

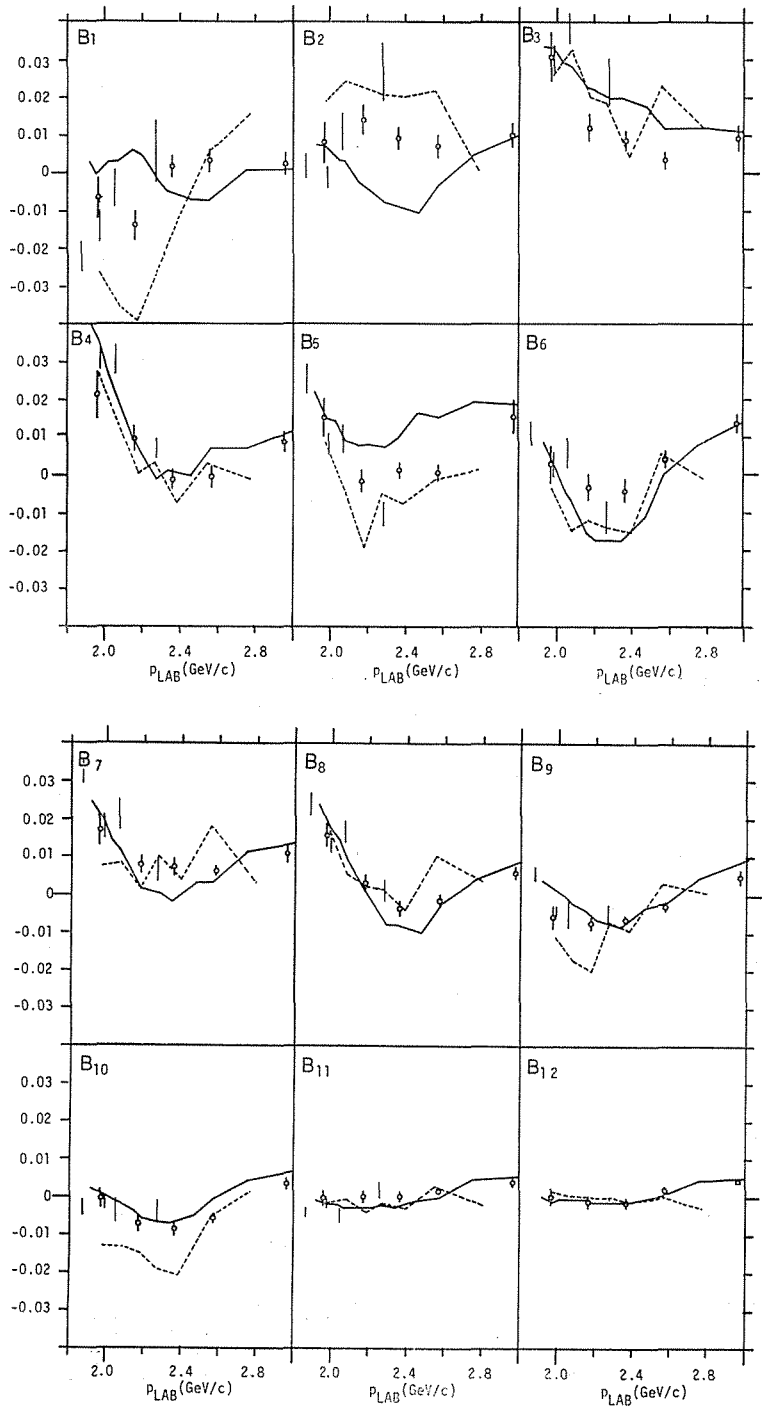

Fig. 25. The Legendre coefficients B_n obtained from the present results (open circle) and from the results of Brown et al. (bar only). The solid lines and the dashed lines indicate the coefficients obtained from the Karlsruhe-Helsinki 78 and the SACLAY 74 solutions, respectively.

Table VIII. Legendre coefficients B_n and χ^2_ν from the fit to the results of this experiment.

p_{LAB}	1.965 GeV/c	2.168 GeV/c	2.360 GeV/c	2.566 GeV/c	2.960 GeV/c
	($\times10^{-4}$)	($\times10^{-4}$)	($\times10^{-4}$)	($\times10^{-4}$)	($\times10^{-4}$)
B_1	-64 ± 53	-137 ± 40	20 ± 27	36 ± 29	27 ± 30
B_2	86 ± 56	139 ± 35	95 ± 23	77 ± 27	109 ± 32
B_3	308 ± 62	124 ± 33	89 ± 23	33 ± 22	91 ± 28
B_4	209 ± 62	95 ± 32	-7 ± 23	-6 ± 22	91 ± 28
B_5	151 ± 54	-14 ± 30	17 ± 25	3 ± 20	158 ± 31
B_6	32 ± 44	-36 ± 30	-40 ± 24	39 ± 17	136 ± 24
B_7	170 ± 33	76 ± 22	73 ± 23	63 ± 12	106 ± 24
B_8	161 ± 26	26 ± 19	-34 ± 18	-17 ± 12	60 ± 22
B_9	-52 ± 24	-69 ± 14	-63 ± 16	-28 ± 9	49 ± 20
B_{10}	0 ± 21	-70 ± 14	-84 ± 13	-54 ± 9	26 ± 15
B_{11}	-2 ± 21	6 ± 14	-2 ± 11	14 ± 9	40 ± 12
B_{12}	-6 ± 20	-17 ± 14	-14 ± 10	17 ± 9	36 ± 11
χ^2_ν	0.70	0.32	2.19	0.53	1.23

Table IX. The χ^2 between B_n's from the results and from the phase shift solutions at each momentum. The solutions Karlsruhe-Helsinki 78 and SACLAY 74 are abbreviated as K–H and SACLAY, respectively. The right-most two columns are the averaged χ^2 over the momenta, where $n=5$ for K–H and $n=4$ for SACLAY.

p_{LAB}	1.965 GeV/c		2.168 GeV/c		2.360 GeV/c		2.566 GeV/c		2.960 GeV/c	$\frac{1}{n}\Sigma\chi^2$	
	K–H	SACLAY	K–H	SACLAY	K–H	SACLAY	K–H	SACLAY	K–H	K–H	SACLAY
B_1	1.04	13.68	24.26	40.01	6.72	30.05	13.36	0.43	0.32	9.14	21.04
B_2	0.08	3.38	20.64	6.32	57.89	23.29	15.71	28.05	0.08	18.88	15.26
B_3	0.13	0.63	10.32	4.76	23.29	4.54	15.64	83.47	0.46	9.97	23.35
B_4	5.93	1.00	0.02	8.45	0.55	9.26	11.93	2.53	0.46	3.78	5.31
B_5	0.00	1.49	9.82	36.80	8.53	12.96	54.02	0.90	0.50	14.57	13.04
B_6	0.00	2.75	14.44	7.29	29.34	21.78	5.26	0.59	0.03	9.82	8.10
B_7	0.83	8.64	4.37	6.95	16.35	1.94	7.56	95.06	1.00	6.02	28.15
B_8	0.53	0.65	0.10	0.03	6.53	0.03	1.17	98.34	1.86	2.04	24.76
B_9	9.00	3.52	4.29	86.22	1.13	5.06	0.79	49.00	4.20	3.88	35.95
B_{10}	0.00	37.74	4.59	31.84	1.16	96.95	23.90	0.31	8.60	7.65	41.71
B_{11}	0.74	0.51	6.61	9.43	6.48	6.95	2.42	4.94	2.78	3.81	5.46
B_{12}	0.49	0.25	0.25	0.86	0.36	0.16	3.57	6.53	1.62	1.26	1.95

In the Fig. 26a, it can be seen that there is a resemblance between the behaviors of ΔB_n and the derivatives with respect to the imaginary part of the H_{11} wave. This feature implies that the discrepancy between B_4^{mes} and B_4^{K-H} at 1.965 GeV/c should be mostly due to the imaginary part of the H_{11} wave.

Similarly, in the Fig. 26b, a clear resemblance is seen between the behaviors of ΔB_n and the derivatives with respect to the imaginary part of the H_9 wave. The same features can be seen at 2.168 and 2.566 GeV/c, too. These features mean that in order to improve the discrepancies between B_1^{mes}, B_2^{mes}, B_3^{mes}, B_5^{mes}, B_6^{mes} and B_1^{K-H}, B_2^{K-H}, B_3^{K-H}, B_5^{K-H}, B_6^{K-H}, respectively, the imaginary part of the H_9 wave should be increased slighly. In this energy region, the H_{19} wave clearly indicates the existence

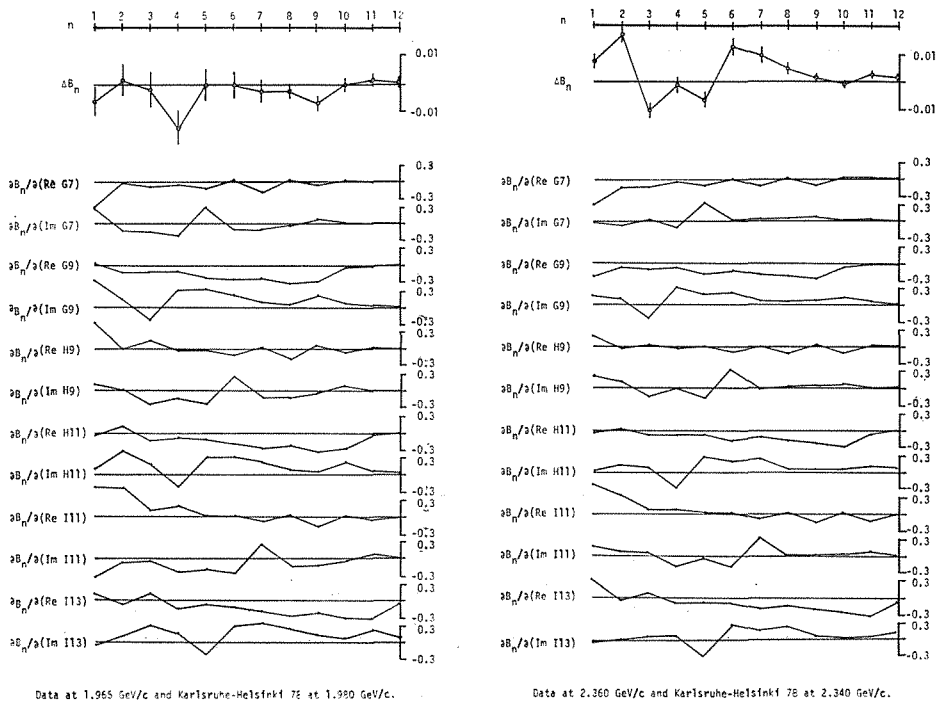

(a) (b)

Fig. 26. The top figure shows the difference of the Legendre coefficients B_n obtained from the Karlsruhe-Helsink 78 solution and those from the present results as a function of n at 1.965 GeV/c (a) and 2.360 GeV/c (b). The derivatives of B_n with respect to the real and imaginary part of the large angular momentum waves are also shown as a function of n.

of the $N(2205)$ resonant state and has the large imaginary part. Therefore, this readjustment of the H_9 wave might modify the resonance parameters of the $N(2205)$ to some extent.

Of course, any single partial wave amplitude cannot be changed alone, because it is related with other waves, and because the change in the charge exchange amplitude will make changes in both of $I=1/2$ and $3/2$ amplitudes to result the effects on the observables for elastic scatterings of $\pi^{\pm}p\to\pi^{\pm}p$.

After all, the phase shift analyses are requested to be done with the results of this experiment together with the new results of the differential cross sections[13] in their input data set in order to see the effects of these features quantitatively and to obtain the improved solution for the π–N phase shifts.

F. Conclusions

The polarization parameters for the π–N charge exchange scattering were measured at the new momentum region between 1.965 and 2.960 GeV/c at almost all angles. The present results at 1.965 GeV/c were in good agreement with the results at 1.975 GeV/c by Brown et al. except in the backward angular region around $\cos\theta^*=-0.45$.

A comparison of the results at the forward region with the Regge pole model with ρ and ρ' exchange exhibits clearly large discrepancies, while the forward differential cross sections at the same momenta are well reproduced with the model in the region of $-t\leqq 1.6$ (GeV/c)^2.

The present results show large discrepancies with the predictions of the phase shift analyses of the SACLAY 74 and Karlsruhe-Helsinki 78 except at 1.965 GeV/c. The results of the Legendre expansion seem to indicate that the partial wave amplitudes H_9 and H_{11} of the Karlsruhe-Helsinki 78 solution might be somewhat modified. The new phase shift analyses are requested including the present results to establish the high mass and high spin resonances in this energy region. The present results will give tight constraints for those new phase shift analyses.

However, the data of the present experiment are of partly poor statistics, and the data are lacking at $\cos\theta^*<-0.9$. A precise measurement of the polarization parameters at the backward angular region is necessary in order to supplement the present results.

ACKNOWLEDGEMENT

The author would like to express his sincere thanks to Prof. K. Miyake and Prof. T. Nakamura for their continuous encouragements and guidance throughout this work. He is deeply grateful to Prof. M. Kobayashi, Dr. R. Kikuchi, Dr. Y. Hemmi, Dr. I. Nakano, Dr. M. Daigo, Mr. Y. Suzuki, Mr. T. Adachi, Mr. S. Naito, Mr. M. Sakuda and Mr. A. Ozaki for their advices and collaboration in carrying out this experiment.

Thanks are also due to Prof. A. Masaike, Prof. K. Morimoto, Dr. S. Hiramatsu, Dr. S. Isagawa and Mr. S. Ishimoto of the Polarized Target Group of KEK for their efforts of constructing the polarized target system and for their valualbe suggestions in operating the target.

The present experiment was performed as the first counter experiment at KEK. Therefore, he is indebted to most of the personnel at KEK, such as the members of the accelerator operation division headed by Prof. Y. Kojima, for the stable operation of the proton synchrotron, those of the beam channel division headed by Prof. H. Hirabayashi for constructing and tuning the pion beam line, those of the counter division headed by Prof. Y. Nagashima for the assistance in preparing the electronics, the data taking computer and the wire spark chambers, those of the data handling division headed by Prof. H. Yoshiki for developing the on-line system and assistance in offiine data analysis and those of the workshop headed by Prof. T. Hongo for fabrication of the detectors and the mechanical instruments.

Finally, he would like to express his sincere thanks to the members of the program coordination room headed by Prof. A. Kusumegi for their proper arrangement in efficient performance of the present experiment and their hospitality.

REFERENCES

1) J. L. Rosner, Phys. Report **11** (1974) 189.
R. J. Cashmore, Proceeding of the 19th International Conference on High Energy Physics, Tokyo (1978) p. 811.
2) R. Ayed and P. Bareyre, Phys. Letters **50B** (1974) 1 (Rev. of Particle Properties).

3) R. E. Cutkosky et al., Contributed paper to the 19th International Conference on High Energy Physics, Tokyo (1978), No. 799.
Phys. Rev. Letters **37** (1976) 645.
4) G. Höller et al., TKP 78–11, TKP 78–12.
E. Pieterinen, Phys. Letters **75B** (1978) 1 (Rev. of Particle Properites).
5) D. D. Drobnis et al., Phys. Rev. Letters **20** (1968) 274.
6) D. Hill et al., Phys. Rev. Letters **30** (1973) 239.
7) P. Bonamy et al., Nucl. Phys. **B16** (1970) 335.
8) P. Bonamy et al., Nucl. Phys. **B52** (1973) 392.
9) J. E. Nelson, LBL–1019 (Ph. D. Thesis).
J. E. Nelson et al., Phys. Letters **47B** (1973) 281.
10) S. R. Shannon, LBL–2607 (Ph. D. Thesis).
S. R. Shannon et al., Phys. Rev. Letters **33** (1974) 237.
11) R. M. Brown et al., Nucl. Phys. **B117** (1976), 12 Nucl. Phys. B137 (1978) 542.
12) R. M. Brown et al., Nucl. Phys. **B144** (1978) 287.
13) Y. Suzuki, The Memoir of the Faculty of Science, Kyoto University, Series A of Physics, Astrophysics, Geophysics and Chemistry **35** (1981) 95.
14) S. Hiramatsu et al., KEK-Preprint–78–8.
15) S. Hiramatsu, to be published.
16) M. Sakuda, Master Thesis (in Japanese).
17) N. Yamashita, The Memoir of the Faculty of Science, Kyoto University, Series A of Physics, Astrophysics, Geophysics and Chemistry **35** (1977) 35.
18) V. Berger and R. J. N. Phillips, Phys. Rev. **187** (1969) 2210.
19) Y. Oyanagi, KEK-Preprint-78–2.
20) G. Höller et al., TKP 78–10.